TITLE PAGE

Full title

The Role of Infarct Transmural Extent in Infarct Extension: A Computational Study

Authors' names, academic degrees, and affiliations

Chin-Neng Leong, BEng[1,2], Einly Lim, PhD[1], Andri Andriyana, PhD[3], Amr Al Abed, PhD[2], Nigel Hamilton Lovell, PhD[2], Christopher Hayward, MBBS, PhD[4], Christian Hamilton-Craig, MBBS, PhD, FACC[5], Socrates Dokos, PhD[2]

[1]Department of Biomedical Engineering, Faculty of Engineering, University of Malaya, 50603 Kuala Lumpur, Malaysia.

[2]Graduate School of Biomedical Engineering, UNSW, Sydney, NSW 2052, Australia.

[3]Department of Mechanical Engineering, Faculty of Engineering, University of Malaya, 50603 Kuala Lumpur, Malaysia.

[4]St Vincent's Hospital, Sydney; UNSW, Sydney; Victor Chang Cardiac Research Institute, Sydney, NSW, Australia.

[5]Centre for Advanced Imaging, University of Queensland, Brisbane, QLD, Australia; University of Washington School of Medicine, Seattle WA, USA.

Corresponding author

Name: Einly Lim

Address: Department of Biomedical Engineering, Faculty of Engineering, University of Malaya, 50603 Kuala Lumpur, Malaysia.

Fax Number: +603-79560027

Telephone Number: +603-79677612

Email: einly_lim@um.edu.my

Acknowledgements

We would like to thank Chee Kok Han, Yang Faridah Abdul Aziz, Shahrul Amry Hashim, and Liew Yih Miin, PhD, for providing valuable consultation, as well as Chan Bee Ting, MS, for helping in construction of the computational models.

ABSTRACT

Infarct extension, a process involving progressive extension of the infarct zone (IZ) into the normally perfused border zone (BZ), leads to continuous degradation of the myocardial function and adverse remodeling. Despite carrying a high risk of mortality, detailed understanding of the mechanisms leading to BZ hypoxia and infarct extension remains unexplored. In the present study, we developed a 3D truncated ellipsoidal left ventricular (LV) model incorporating realistic electromechanical properties and fiber orientation to examine

This article has been accepted for publication and undergone full peer review but has not been through the copyediting, typesetting, pagination and proofreading process which may lead to differences between this version and the Version of Record. Please cite this article as doi: 10.1002/cnm.2794

the mechanical interaction among the remote, infarct and border zones in the presence of varying infarct transmural extent (TME). Localized highly abnormal systolic fiber stress was observed at the BZ, owing to the simultaneous presence of moderately increased stiffness and fiber strain at this region, caused by the mechanical tethering effect imposed by the overstretched IZ. Our simulations also demonstrated the greatest tethering effect and stress in BZ regions with fiber direction tangential to the BZ-RZ boundary. This can be explained by the lower stiffness in the cross-fiber direction, which gave rise to a greater stretching of the IZ in this direction. The average fiber strain of the IZ, as well as the maximum stress in the subendocardial layer increased steeply from 10% to 50% infarct TME, and slower thereafter. Based on our stress-strain loop analysis, we found impairment in the myocardial energy efficiency and elevated energy expenditure with increasing infarct TME, which we believe to place the BZ at further risk of hypoxia.

Keywords: infarct extension; infarct transmural extent; border zone; finite element modeling

INTRODUCTION

Myocardial infarction (MI) affects more than 7 million people each year worldwide, and remains as one of the most common causes of morbidity and mortality [1]. Following MI, the left ventricle (LV) undergoes physiological changes in response to alterations in myocardial load to maintain cardiac homeostasis [2]. However, these physiological changes can be pathological, resulting in degeneration of myocardial function and adverse remodeling of the LV over time, eventually giving rise to heart failure. Nearly 70% of heart failure cases are due to LV remodeling following MI [3]. Prediction and prevention of remodeling events are therefore important in reducing rates of MI patient morbidity and mortality.

Infarct expansion involves radial thinning, circumferential lengthening and dilation of the non-contractile infarct region, which occur during a timeframe of days to weeks after an acute MI. Infarct expansion has adverse effects on LV function and contractility of the residual myocardium, possibly resulting in infarct rupture, ventricular dilation and aneurysm [4]. Infarct extension, on the other hand, takes place over a timeframe of weeks to months following MI, and represents another complication associated with ventricular remodeling. Infarct extension involves reinfarction of the normally perfused border zone (BZ) adjacent to the infarct, which subsequently extends the infarct zone (IZ) progressively, and at the same time drags the neighboring myocardium into the BZ [5]. Patients with infarct extension have an in-hospital mortality more than four times higher than those without extension [6]. Furthermore, increasing the amount of transmural necrosis following infarct extension can cause infarct expansion and its related complications. The combined effects of infarct expansion and extension give rise to the feed-forward cycle of the remodeling process, resulting in continuous cardiomyocyte apoptotic and necrotic death, ventricular thinning and dilation [7].

Infarct transmural extent (TME) or transmurality, is defined as the volumetric penetration of the infarct from the endocardium towards the epicardium, and has been shown in past studies to be an important determinant of the occurrence of remodeling events. Although hemorrhagic infarction segment count and infarct size have also been correlated with the occurrence of remodeling, Ahn et al. and Berti et al. demonstrated through multivariate regression analysis that infarct TME was the only independent indicator of remodeling [8,9]. Using echocardiographic assessments of myocardial viability, Kaul and co-workers demonstrated the pivotal role of viable subepicardium in preventing dilation and thinning of the infarct, which subsequently preserved LV shape, as well as inhibiting infarct expansion

[10]. Although the influence of infarct TME towards infarct expansion is well known, the correlation between infarct TME and events underlying infarct extension at the BZ remains unanswered. From a mechanical perspective, the occurrence of infarct extension can be understood as the presence of highly abnormal stress at the BZ owing to mechanical "tethering" between the normal and ischemic myocardium [4,11]. Nevertheless, unlike infarct expansion, detailed exploration of the mechanisms underlying infarct extension, which involves the interaction between the remote zone (RZ) and IZ, as well as the resultant highly abnormal stress at the BZ, is still lacking. Furthermore, the role of infarct TME in such interaction remains unclear. Likewise, the importance of local fiber orientation on the presence of high stress at the BZ has not been explored.

We have seen much improvement in imaging techniques in the past decades. Tagged and diffusion tensor cardiovascular magnetic resonance imaging (CMR) are capable of quantifying LV regional strains [12] and fiber orientation [13] respectively, whilst late gadolinium enhancement (LGE) CMR renders non-invasive measurement of infarct zone a reality [14]. However, regional mechanical function such as LV wall stress, remains out of reach. Although Laplace law has been a preferred means of quantification of LV wall stress, it does not take into account the varying LV tissue properties and fiber orientation, leading to inaccurate wall stress calculation [15]. The use of the computational finite element (FE) method is essential in comprehending the mechanical function of the infarcted LV, since it offers a more complete visualization of LV regional mechanics. Over the last few decades, there has been much improvement in LV modeling, imaging techniques and computational power facilitating personalized patient-specific simulations. FE models have been employed in earlier studies to examine the effects of MI size [16] and mechanical properties [17] on LV function. Although Shimkunas, Wenk and colleagues successfully used their patient-specific LV models to demonstrate the depressed contractility of BZ after MI [3,18], limited attention has been paid to the correlation of impaired mechanics with infarct extension at the BZ following MI.

In the present study, FE computations were carried out using simplified 3D ellipsoidal electro-mechanical LV models to examine the effect of infarct TME on localized stress, which is believed to be a causal factor of infarct extension and remodeling at the BZ. Simulations of a complete LV cycle were performed for models of varying infarct TME, keeping the electrophysiological and mechanical properties of IZ, BZ and RZ fixed. The mechanisms underlying highly abnormal stress distribution was investigated from a mechanical viewpoint. In particular, we studied how mechanical interaction between normal and ischemic myocardium contributed to impaired BZ mechanics, taking into account the importance of local fiber orientation.

METHODS

A. Geometry

The LV was modeled as a truncated 3D ellipsoid (see Fig. 1A), with an inner cavity short-to-long axis length ratio of 0.5, a cavity volume of 65 ml and a truncated base opening of 3 cm diameter to represent the valve annuli [2]. The wall thickness at the base and apex of the LV model was assigned to values reported in a previous study [19]. All model dimensions are given in Table 1, and the definition of circumferential (C_S), longitudinal (L_S) and radial (R_T) directions are shown in Fig. 1B.

B. Electrophysiology Formulations

Action potential (AP) propagation from LV apex to base was simulated by using modified FitzHugh-Nagumo equations adopted from Nash and Panfilov [20]:

$$\frac{\partial V}{\partial t} = \left(\sum_{i=1}^{3} \sum_{j=1}^{3} \frac{\partial D_{ij}}{\partial x_i} \frac{\partial V}{\partial x_j} \right) - kV(V-a)(V-1) - crV + cI_s \quad (1)$$

$$\frac{\partial r}{\partial t} = (\varepsilon + \frac{\mu_1 r}{\mu_2 + V})[-cr - kV(V-b-1)] \quad (2)$$

where V is the dimensionless transmembrane potential with normalized amplitude between 0 and 1, and r represents a dimensionless conductance of a slow inward current which manipulates the recovery of V and serves to activate the onset of t_s (s), a variable representing the active contraction onset time of the myocardium:

$$\frac{\P t_s}{\P t} = \begin{cases} 1 & r > 0.002, \\ 0 & otherwise \end{cases} \quad (3)$$

Parameters, a, b, c (s^{-1}), k (s^{-1}), ε, μ_1 and μ_2 regulate AP shape and restitution properties, and I_s is a dimensionless external stimulus current, which was applied at the LV apex to initiate active contraction. The x_i and x_j are unit vectors of local orthogonal coordinate system axes, whilst D_{ij} (m^2/s) is the electrical conductivity of myocardium given by:

$$D_{ij} = f_i f_j D_f + s_i s_j D_t + r_i r_j D_t \quad (4)$$

where D_f (m^2/s) and D_t (m^2/s) are the fiber and cross-fiber conductivities respectively. The coefficients f, s and r represent the projection of fiber, sheet-fiber and radial base vectors respectively, onto base vectors denoted by their subscripts, i and j.

C. Mechanics Formulations

The passive mechanical properties of the myocardium were modeled as a quasi-static, nearly-incompressible hyperelastic material using a non-linear strain energy function, W (kPa). Transversely isotropic behavior was assumed, aligned with the local fiber direction which varied transmurally from +60° to -60° (endocardium to epicardium) with respect to the circumferential direction [21], as shown in Fig. 1C. The nearly-incompressible characteristic was imposed by the Lagrangian multiplier, p (MPa):

$$W = \frac{1}{2} C_0 (e^Q - 1) + p(J-1) \quad (5)$$

where C_0 (kPa) represents the overall stiffness of the myocardium and J is the determinant of the deformation gradient tensor, equals to 1 for volume-preserving strains. Q was expressed in terms of the local strain components as:

$$Q = b_f E_{ff}^{\ 2} + b_t (E_{ss}^{\ 2} + E_{rr}^{\ 2} + 2E_{sr}^{\ 2}) + 2b_{fa} (E_{fs}^{\ 2} + E_{fr}^{\ 2}) \quad (6)$$

where the E_{ij} represent components of the Green-Lagrange strain tensor, with f, s and r subscripts denoting the local fiber, sheet-fiber and radial directions, respectively. The parameters, b_f, b_t and b_{fa} describe the exponential stress-strain relation of the material.

Active contraction of the LV was modelled by adding stress defined as an active tension component, T_a (kPa), in the myocardial fiber direction, with 40% of T_a added to the stress in the cross-fiber directions [22]:

$$S_{ij} = \frac{\partial W}{\partial E_{ij}} + \left(0.6\delta_{if}\delta_{fj} + 0.4\delta_{ij}\right)T_a \qquad (7)$$

where S_{ij} denotes the i,j th component of the second Piola-Kirchoff stress tensor ($i, j = f, s, r$), δ is the Kronecker delta, and T_a is given by:

$$T_a = A\frac{t_s^2}{\tau}e^{-\frac{t_s^n}{\tau}} \qquad (8)$$

where t_s (s) denotes the local onset time of active contraction, as described in Eq. (3). A defines the amplitude of T_a, whilst τ and n determine the onset and offset rates:

$$\begin{aligned} A &= T_0[A_3 l^3 + A_2 l^2 + A_1 l + A_0] \\ \tau &= \tau_0[m_\tau l + c_\tau] \\ n &= n_0[m_n l + c_n] \end{aligned} \qquad (9)$$

Parameters, T_0 (kPa), A_3 (μm^{-3}), A_2 (μm^{-2}), A_1 (μm^{-1}), A_0, τ_0, m_τ (μm^{-1}), c_τ, n_0, m_n (μm^{-1}) and c_n are the coefficients of polynomial functions of A (kPa), τ and n, with l (μm) denoting the local sarcomere length expressed as:

$$l = l_0\sqrt{2E_{ff} + 1} \qquad (10)$$

with l_0 (μm) representing the reference sarcomere length at zero strain.

D. Boundary Conditions

The basal surface of the LV was fixed to account for the effect of the left atrium and the valve annuli. For simplicity, no pressure was applied on the epicardial surface, as in similar past FE studies [2,3]. In diastole, an LV pressure, *plv* (mmHg) of 8 mmHg was imposed on the endocardial surface of the LV. To simulate isovolumic contraction (IVC), the volume of the LV cavity, *vlv* (ml) was held constant, whilst *plv* was solved concurrently as an additional variable associated with this constant-volume constraint. The end of IVC was assumed to be reached when *plv* achieved 80 mmHg, at which instant the aortic valve was assumed to open. In simulating the subsequent ejection phase, the isovolumic constraint boundary condition was replaced by a 3-element Windkessel model to compute the *plv* associated with the effect of blood ejection:

$$plv = P_A + Q_A R_c \qquad (11)$$

$$C_p\frac{dP_A}{dt} + \frac{P_A}{R_p} - Q_A = 0 \qquad (12)$$

where P_A (mmHg) represents the distal arterial blood pressure and Q_A (ml/s) denotes the rate of blood flow being ejected from the LV (i.e. cardiac output). R_c (mmHg.s/ml), R_p (mmHg.s/ml) and C_p (ml/mmHg) are the Windkessel model aortic root impedance, peripheral impedance and peripheral capacitance respectively. The ejection phase ended when P_A was greater than *plv*, at which point the aortic valve was assumed to close. In the following isovolumic relaxation (IVR) phase, an isovolumic constraint boundary condition similar to the IVC phase was used to replace the Windkessel model. The IVR phase was assumed to be complete when *plv* reached 0 mmHg, at which instant the mitral valve opened. Finally, early diastole was simulated by applying a *plv* of 0 mmHg on the endocardial surface of the LV model, such that it returned to its reference (i.e. zero-strain) state. The model was solved using the COMSOL v4.4 finite-element software package (COMSOL AB, Sweden).

E. Parameter Values

Parameter values of the above equations are listed in Table 1. The constants c and k were adjusted to reproduce cardiac AP physiological shape and restitution duration. D_f and D_t were tuned to reproduce the ratio of fiber to cross-fiber conduction speed reported in the study of Potse et al. [23], as well as reported physiological activation time of the whole LV (nearly 40 ms) [24]. The overall stiffness of the myocardium, C_0 was set such that LV end diastolic volume (EDV) equaled 118.7 ml as reported by Lee et al. [19]. The values of stress-strain parameters, b_f, b_t and b_{fa} were adopted from Wenk et al. [3]. Parameters used in the formulation of T_a (i.e. A_3, A_2, A_1, A_0, m_τ, c_τ, m_n and c_n) were first optimized to reproduce the active tension curves reported by Rice et al. [25]. Parameters τ_0 and n_0 were then further tuned to regulate the onset and offset rate of T_a, together with the optimization of the Windkessel model input parameters (R_c, R_p and C_p), to produce physiological *plv* and *vlv* values comparable to a standard Wigger's diagram [26]. T_0 was regulated to reproduce previously reported end systolic volume (ESV) [19]. The full cycle trajectories of *plv* and *vlv* of the LV model are shown in Fig. 2.

F. Infarct Models

In our recently published study based on simulations using varying infarct sizes, we found that the major factor affecting LV mechanics was infarct TME rather than size [27]. Therefore, only one infarct size was chosen to be simulated in the present study. Whilst introducing the infarct, its shape was kept rounded (to avoid sharp edges which could affect stress distribution), and at the same time it was kept some distance away from the basal surface and the apex (to avoid boundary condition effects). With these criteria, a relative infarct size of 14.3% was obtained (calculated from endocardial infarct area divided by total endocardial area), which is within the normal range of infarct size [8].

To examine the effect of infarct TME on LV regional mechanics, five infarct models with varying infarct TME were built from the normal model (**NORMAL**): 10% (**TR10**), 24% (**TR24**), 51% (**TR51**), 75% (**TR75**) and 100% TME (**TR100**), with infarct volume, endocardial covered area and TME of the models given in Table 2. The TME of the infarct was calculated by:

$$TME = \frac{Infarct\ Volume}{Endocardial\ Area\ Covered \times Basal\ Wall\ Thickness} \times 100\% \quad (13)$$

The infarcts were considered as transmural (**TR51**, **TR75** and **TR100** models) if the TME exceeded 50%, and non-transmural (**TR10** and **TR24** models) otherwise [28]. These generated infarct models are shown in Fig. 3. The IZ was approximated as having a three-fold passive stiffness to that of the RZ, in accordance with its reportedly higher elasticity at six-weeks [29,30], the time frame over which infarct extension is believed to occur. To account for the lower electrical conductivity of the IZ, conductivity parameters, D_f and D_t were manually tuned such that the ratio of the conduction velocity of IZ to RZ matched the results of Abd-Elmoniem et al. [31]. In regard to its active contractile property, the IZ was assumed to have zero contractility (T_0 = 0 Pa), corresponding to its non-contractile property [3]. The BZ properties (C_0, D_f, D_t, and T_0) were modeled as transitioning from the RZ to the IZ following the pattern illustrated in Fig. 3.

The geometry was meshed with quadratic tetrahedral elements. The mesh size was then adjusted until the average IZ fiber strain for model **TR100** at end-systole changed by less than 1%. It was found that a total number of 10833 tetrahedral elements, with a maximum element size of 5.69 mm were sufficient for the present study. Figs. 1D, 1E and 1F show the

undeformed mesh as well as the deformed meshes of the **NORMAL** model at end-diastole and end-systole, respectively. The resulting non-linear equations were solved monolithically using the PARDISO solver with generalized alpha time stepping method in COMSOL (v4.4, COMSOL AB, Sweden). An absolute tolerance of 1.0×10^{-3} and a time step of 5 ms were used for the simulations of the cardiac cycles. The models were solved using an Intel Xeon E5-2620 6-core 2.00 GHz processor with a 64 GB of RAM and took nearly seven hours to compute a complete cardiac cycle.

To ensure the physiological relevance of our generated models, we evaluated the performance of our models by comparing the resultant circumferential strain trajectories of various myocardial layers against that obtained from past clinical studies. In order to elucidate the impairment of BZ myocardial mechanics as a function of infarct TME, mechanical interaction between RZ, BZ and IZ was analyzed for the generated infarct models. The effect of fiber orientation on this interaction was studied by comparing fiber stress against the difference in angle between the myocardial fibers and the BZ-RZ boundary. Subsequently, stress-strain loops were used to indicate BZ myocardial stroke work density, which reveals the energy expenditure and efficiency of the myocardium at the BZ. Such myocardial energy expenditure and efficiency could infer, at least in part, possible long-term deterioration of the LV function [32].

RESULTS

Fig. 4 illustrates the activation times of the subendocardium (17% wall thickness radial from endocardium) and subepicardium (83% wall thickness radial from endocardium) for the **NORMAL** and **TR100** models. In both myocardial layers, delay of activation was not seen at the apex region of the infarct model. However, at the basal and mid regions of this model, an approximately 10 ms delay in activation was observed at the BZ and RZ. The greatest delay of up to nearly 35 ms was observed at the upper part of the IZ for the **TR100** model relative to the **NORMAL** model.

Simulated EDV, ESV, stroke volume (SV) and ejection fraction (EF) of the models are listed in Table 3. The infarct TME affected ESV more than EDV, resulting in an increase of 9.1 ml in ESV and a decrease of 3.9 ml in EDV from the **NORMAL** to the **TR100** case. The SV, EF and peak systolic pressure (P_{sys}) declined as infarct TME increased, with a 13.0 ml, 9% and 14.4 mmHg reduction in the **TR100** model relative to the **NORMAL** model, respectively.

To illustrate the time course of circumferential strain for various myocardial layers (subendocardium, mid-myocardium and subepicardium), a point from each layer of the infarct segment was selected as shown in Fig. 5A for the plots. For better presentation of the myocardial strain during contraction, the early ejection phase was chosen as the starting point for these plots. As can be seen in Fig. 5B, the absolute magnitude of systolic strain declined when moving from the subendocardial to the subepicardial layer. At the subendocardial layer, the systolic strain was impaired in all infarct models, with a greater impairment with increasing levels of infarct TME. Conversely, in the mid-myocardial and subepicardial layers, impairment of systolic strain was only pronounced in the transmural infarct models. In these transmural infarct models, the systolic strain at all three layers was depressed with increasing infarct TME.

The progression of the end systolic (ES) fiber strain and stress distributions from the IZ to the BZ and RZ were generated to visualize the mechanical interaction among the three zones. To do this, the fiber strain and stress distributions were plotted along rings spanning around

the subendocardium and subepicardium, as shown in Figs. 6A and 6C respectively. As the subendocardial layers of both non-transmural and transmural models (presented by **TR24** and **TR100** models respectively) were infarcted, the fiber strain was highly elevated at the IZ of both models. Meanwhile, the myocardium progressed from being non-contractile at the IZ-BZ boundary to contractile at the BZ-RZ boundary, as shown in Fig. 6B. Contrary to the subendocardium, the infarct extended to the subepicardium layer only in the transmural model. Abnormally high strain was thus observed only at the subepicardium layer of the **TR100** model, as illustrated in Fig. 6D, with the transition from non-contractile to contractile occurring at the BZ. Consequently, highly abnormal stress was observed at the subendocardial layer of both **TR24** and **TR100** models, and at the subepicardial layer of the **TR100** model only.

To study the effect of fiber orientation on stress distribution, ES fiber stress for the subendocardial and subepicardial layers of model **TR100** was generated, as shown in Figs. 7A and 7B respectively, alongside arrows representing the local fiber orientation. As can be seen, the fiber stress distributions for both layers were non-homogeneous, particularly at the BZ. Fig. 7C presents the correlation between the fiber stress and the angle difference between the myocardial fiber and the BZ-RZ boundary. As shown in the figure, the fiber stress was highest at region where the myocardial fiber was tangential to the BZ-RZ boundary (indicated by the 0^{o} angle difference). In contrast, much lower stress was obtained at areas with fiber orientation perpendicular to the BZ-RZ boundary. To examine whether these stresses were due to an improper enforcement of material incompressibility (since we used a nearly-incompressible framework), we inspected the resulting volumetric strain throughout the myocardium. Most regions exhibited a volumetric strain of 1 (i.e. incompressibility), with the exception of only small localized regions near some parts of the IZ-BZ boundary with volumetric strains ranging from 0.7-1.4, likely due to errors in mesh discretization. These regions, however, were small and did not systematically correspond to the regions of high fiber stress shown in Fig. 7. These high fiber stresses did not therefore result from variations in volumetric strain.

Figs. 8A and 8B illustrate the stress-strain loops of the simulated models, taken from the maximum fiber stress points in the subendocardial and subepicardial layers, respectively. As shown, as infarct TME increased, the stress-strain loops became less rectangular with greater maximum stress, in both myocardial layers. The only exception was the stress-strain loop of the subendocardial layer for the **TR100** model which appeared to fall between those for the **TR24** and **TR51** models.

To demonstrate the importance of viable subepicardium in preserving the shape of the LV, ES fiber strain in the short axis view was plotted for each model (Fig. 9A). The fiber strain at the IZ was generally elevated with increasing level of infarct TME. Dilation of the IZ can be seen in the transmural infarct models as indicated by the impaired circular shape of the model cavities.

The average fiber strain of the IZ, as well as the maximum fiber stress in the subendocardial and subepicardial layers with increasing infarct TME level is illustrated in Fig. 9B. The average fiber strain of the IZ increased by 0.089 from 10% to 51% of infarct TME level and started to saturate beyond that, with an increase of only 0.013 from 51% to 100% TME level. With regards to the maximum stress in the subendocardial layer, its magnitude increased by 196 kPa from 10% to 51% of infarct TME level, followed by a rise of 37 kPa from 51% to 75% of infarct TME, and dropped by 113 kPa at 100% TME level. Meanwhile, the maximum fiber stress in the subepicardium rose linearly with increasing infarct TME, and its magnitude was generally lower relative to that of the subendocardial layer at all levels of

infarct TME. The transmural gradient of rotation of the myocardium with maximum fiber stress was derived along the dashed line illustrated in Fig. 9C. It was observed that the subendocardial maximum stress followed the trend of transmural gradient of rotation with increasing TME of the infarct, as depicted in Fig. 9D.

DISCUSSION

The results of this study showed that infarct TME contributed substantially to the highly abnormal stress distribution and impaired mechanics at the BZ, which are believed to contribute to infarct extension and remodeling. New findings included the importance of mechanical interaction between ischemic and viable myocardium, as well as the contribution of fiber orientation in such interaction.

Comparison of Model Performance

In a recent clinical study using echocardiography on fifty-six patients, Becker et al. demonstrated that the impairment of circumferential strain was only pronounced in the subendocardium, with only minor impairment observed in the mid myocardium and subepicardium of non-transmural infarcted LV. With regards to transmural-infarcted LV, the circumferential strain was reduced in all the three layers of myocardium. The same findings were also observed in our simulated models. Furthermore, the time course of circumferential strain, as well as its regression of magnitude change from the subendocardial to the mid-myocardial and the subepicardial layers (Fig. 5B), showed good agreement with the circumferential strain tracings reported in the study of Becker et al. [28], thus supporting the physiological relevance of our generated models.

Mechanical Interaction among IZ, BZ and RZ

It was believed that the mechanical tethering effect of the IZ on the BZ gave rise to abnormally high stress in the BZ, which subsequently led to infarct extension [11]. Since mechanical interaction operates in both directions, the mechanical tethering was imposed on both the IZ and BZ. However, high stress and infarct extension were only observed at the BZ but not at the IZ and RZ. Based on our results (Fig. 6), BZ and its surrounding myocardium were the only regions with elevated fiber stress, with strain levels lying between the myocardium of the other two zones. Mechanically, high fiber stress is present only when a large fiber strain is applied to a stiff myocardium. The presence of high BZ strain and contractility ("stiffness" during active contraction) explains the abnormally high stress observed at this region. On the contrary, this phenomenon was not observed in either the IZ or RZ owing to the low stiffness of the IZ and the diminished strain at the RZ.

Another important finding of the present study is the role played by fiber orientation on the non-homogeneous distribution of ES fiber stress, with greatest stress recorded in regions with fiber orientation tangential to the BZ-RZ boundary (Fig. 7). This can be explained by the difference in stiffness between the fiber and cross-fiber directions. Since the myocardial wall is stiffer in the fiber direction ($b_f > b_t$), the IZ was stretched unevenly, with greater stretching occurring in the cross-fiber direction. As a result, BZ regions with fiber direction tangential to the BZ-RZ boundary bore the greatest tethering effect, thus yielding the highest stress. In short, it was the mechanical tethering or interaction among the three zones, together with the simultaneous presence of moderately high strain and contractility at the BZ, as well as the fiber orientation at the IZ, that gave rise to the localized abnormally high stress pattern at the BZ.

Correlation between Infarct TME and its Extension

Kaul et al. demonstrated the crucial role played by the viable subepicardial layer in preventing the IZ from dilating and thus maintaining the shape of the LV [10]. In transmurally infarcted LV, the surviving contractile subepicardium was no longer adequate to withstand the outward pressure imposed by the IZ. As a result, the IZ began to dilate and demonstrate an elevated fiber strain (Figs. 9A and 9B). This explains the observations from recent studies [9] which found a higher risk of infarct expansion events in transmurally infarcted LVs. As our results demonstrated that localized highly abnormal stress at the BZ was a result of mechanical tethering following an overstretched IZ (Fig. 6), the magnitude of the maximum fiber stress recorded at both the subendocardial and subepicardial layers was also found to have a positive correlation with average IZ fiber strain (Fig. 9B). One exceptional case was found at the subendocardium layer of model TR100, where the maximum stress dropped despite an increase in average infarct strain with increasing TME.

Our further analysis showed that the transmural gradient of rotation was closely correlated with maximum stress recorded at the subendocardial layer, and may explain the unexpected decline of maximum stress for model **TR100**. The transmural gradient of rotation measures the sliding of the neighboring myocardial sheets against each other, and is responsible for the shear stress imposed on the myocardium. Due to a gradual change in the fiber orientation from +60° at the subendocardial layer to -60° at the subepicardial layer, the rotation of the subepicardial layer was counteracted by the subendocardial layer [33]. However, as the subepicardial layer exhibited a larger radius and volume, it determined the overall rotation of the LV wall. In model **TR100** with infarction spanning across the entire wall thickness, the resultant transmural gradient of rotation was depressed, and thus a reduction in the maximum stress was recorded at the subendocardial layer. Nevertheless, a fully transmural infarcted LV (as represented by model **TR100**) can still be a major concern because its infarct expansion can chronically augment the mechanical tethering and thus the stress imposed on the BZ.

The stress-strain loop has been used to indicate the stroke work density, which reveals the energy expenditure and efficiency of the myocardium [32]. A less rectangular loop represents lower myocardial energy efficiency, whilst a greater loop area signifies higher myocardial energy expenditure. Although Wenk, Shimkunas and colleagues successfully demonstrated a depressed contractility in the BZ after the occurrence of MI [3,18], the subsequent complications associated with depressed contractility were not discussed. Based on our simulation results (Figs. 8A and 8B), the myocardial energy efficiency was shown to decline while the energy expenditure increased with increasing infarct TME. Therefore, apart from the depressed contractility and high stress at the BZ, we believe that impaired energy efficiency and elevated energy expenditure were also accountable for the higher risk of infarct extension in transmurally infarcted LVs.

LV Activation and Global Function

In spite of delayed activation at the LV base and mid region of model **TR100**, the activation at the BZ was not delayed compared to that of the RZ, whilst a pronounced activation delay was observed at the IZ. In contrast, systolic function of the BZ was found to be depressed compared to that of the RZ. From the mismatch between regions with depressed systolic function and delayed activation (Figs. 4 and 7), we suggest that infarct extension at the BZ is most likely contributed solely by altered LV mechanical function instead of electrophysiological factors. The same finding was also reported in a recent study by Ashikaga et al. using a high resolution CMR technique [11].

LV global function, though depressed with increasing infarct TME, fell within the normal or mildly abnormal range [34] for all models simulated in the present study (Table 3). This observation suggested that regional impairment of the LV, including myocardial strain and stress overloads, might be masked by global indices of LV function. LV remodeling can still occur in spite of normal global LV function [35]. Therefore, the global indices should not be the only determinants for prediction of remodeling events following MI.

Clinical Significance

As discussed above, following an acute MI, particularly in the transmurally infarcted LV, the interaction between the IZ, BZ and RZ gave rise to the concentration of BZ high stress, impaired efficiency and elevated energy expenditure. Prolonged, severe stress overload leads to excessive forms of collagen deposition or fibrosis, which diminishes the capillary density and amplifies the oxygen diffusion distance. This, together with the increased energy expenditure and reduced energy efficiency, placing the BZ myocardium at further risk of hypoxia [36]. With severely affected myocardial metabolism, the BZ becomes more susceptible to apoptosis and infarct extension, a process in which the BZ turns into ischemic myocardium and becomes part of the IZ. Meanwhile, the BZ extends to its neighboring RZ [5,36]. The combined complications of infarct expansion and extension contribute to the feed-forward cycle of LV remodeling, which involves slippage, apoptotic and necrotic cell death, changes in the myocardial interstitium, a diminished wall thickness and LV dilation, as well as an elevated wall stress [7].

From a mechanical perspective, overstretching of the infarct is accountable for both infarct expansion and extension. Thus, any interventions that aim to inhibit bulging and dilation of the infarct, such as a cardiac support device [37], polymer injection [38] and patching [39], are believed to help prevent or delay the corresponding LV remodeling events. These interventions should not only focus on inhibiting infarct expansion, but should also consider preventing infarct extension. To ensure long-term successful outcomes, these interventions should take into account the relative stiffness of the fiber to cross-fiber direction at the IZ and seek ways to obtain a more homogenous stress distribution at the BZ, as our simulation results showed that fiber orientation plays an important role in producing high stress at the BZ, which may lead to infarct extension.

Model Limitations

A simple truncated ellipsoid was used to model the LV in the present study, which lacked patient-specific validation, and therefore was subject to inaccuracies in geometry and material properties. Such inaccuracies, especially the relative IZ stiffness, might affect the extent of connectivity between ischemic and viable myocardium, and subsequently the quantitative results for stress and strain. However, we believe that the major qualitative findings of our study would not be affected, since the mechanical tethering mechanism between the ischemic and the viable myocardium, the bulging of the IZ and the impaired mechanical energy efficiency of the myocardium with increasing TME, as well as the effect of fiber directionality would all still be exhibited, regardless of inaccuracies in the geometry and the material properties. Therefore, we believe that our simplified model was sufficient to meet the purpose of this study, namely to investigate the qualitative impacts of infarct TME on regional LV mechanics. Furthermore, the quantitative comparison between our simulation results with published findings were not our focus, since to date, threshold values of strain and stress for the initiation of infarct expansion and extension remain unclear.

Residual stresses, which are present in the myocardium, were not included in our models. However, as shown in the results, the myocardial mechanics was most impaired during end-

systole, at which instant the LV pressure was much greater than the residual stresses imposed on the myocardium. Thus, we strongly believe that the effects of residual stresses are minimal, particularly during end-systole, and are unlikely to alter our major findings.

The dynamics of myocyte twitch tension in our models was modulated by myocyte sarcomere length throughout the systolic phase, without incorporation of a force-velocity relationship. The main reason was that LV myocyte force-velocity relationship for humans, or species with similar LV anatomy to humans, is still lacking to date [40]. We assumed that the decrease of the sarcomere length and corresponding decrease in twitch tension during contraction were adequate in representing the force-velocity relationship of the myocyte. In addition, we demonstrated that the time course of myocardial circumferential strain in our models matched well with observations in a previous study [28].

It has been shown in previous studies that mechano-electric feedback following infarction could elevate effective refractory period [41] and AP dispersion [42], which subsequently leads to electrophysiology-related complications such as arrhythmias, current reentry and tachycardia [43]. However, since the focus of the present work was on the impairment of LV mechanical function following MI, incorporating variations in myocyte electrophysiological properties within the infarct as well as mechano-electric feedback, along with their corresponding complications, were beyond the scope of this study. Therefore, the modified FitzHugh-Nagumo model was assumed sufficient in simulating AP propagation. Other diseases, such as mitral regurgitation and LV outflow tract obstruction, which may occur following an MI event, were also beyond the scope of this study.

Conclusions and Future Work

We have demonstrated in the present study that infarct TME is an important determinant for the existence of highly abnormal stress, elevated myocardial energy expenditure and impaired myocardial energy efficiency at the BZ, which are believed to put the LV at a higher risk of infarct extension. In addition, our simulation results suggested that impaired myocardial mechanics at the BZ was a consequence of the combined effects of mechanical tethering, the simultaneous presence of moderately high strain and contractility at this region, as well as the fiber orientation at the IZ. In future, the geometry of our model will be modified to be patient-specific, allowing more accurate prediction and quantification of the simulated variables, since optimization of model parameters could be performed accurately using patient-specific data such as myocardial movements extracted from the cine, tagged and LGE CMR images. Moreover, current study focused only on altered regional mechanical LV function following an MI event, further studies are required to investigate the electrophysiological and mechano-electric feedback factors, as well as the importance of myocardial transmural heterogeneity.

ACKNOWLEDGMENTS

We would like to thank Chee Kok Han, Yang Faridah Abdul Aziz, Shahrul Amry Hashim, and Liew Yih Miin, PhD, for providing valuable consultation, as well as Chan Bee Ting, MS, for helping in construction of the computational models.

SOURCES OF FUNDING

This study was supported by the Ministry of Higher Education of Malaysia (UM.C/HIR/MOHE/ENG/50) and University of Malaya Research Grants (RP028-14HTM).

DISCLOSURES

No conflicts of interest, financial or otherwise, are declared by the authors.

REFERENCES

1. White HD, Chew DP. Acute myocardial infarction. *The Lancet* 2008; **372(9638)**: 570-584.
2. Choi HF, Rademakers FE, Claus P. Left-ventricular shape determines intramyocardial mechanical heterogeneity. *American Journal of Physiology-Heart and Circulatory Physiology* 2011; **301(6)**: H2351-H2361.
3. Wenk JF, Klepach D, Lee LC, et al. First evidence of depressed contractility in the border zone of a human myocardial infarction. *The Annals of Thoracic Surgery* 2012; **93(4)**: 1188-1193.
4. French BA, Kramer CM. Mechanisms of postinfarct left ventricular remodeling. *Drug Discovery Today: Disease Mechanisms* 2007; **4(3)**: 185-196.
5. Walker JC, Ratcliffe MB, Zhang P, et al. Magnetic resonance imaging-based finite element stress analysis after linear repair of left ventricular aneurysm. *The Journal of Thoracic and Cardiovascular Surgery* 2008; **135(5)**: 1094-1102.
6. Ratcliffe MB. Non-ischemic infarct extension: A new type of infarct enlargement and a potential therapeutic target. *Journal of the American College of Cardiology* 2002; **40(6)**: 1168-1171.
7. Diwan A, Krenz M, Syed FM, et al. Inhibition of ischemic cardiomyocyte apoptosis through targeted ablation of Bnip3 restrains postinfarction remodeling in mice. *The Journal of Clinical Investigation* 2007; **117(10)**: 2825-2833.
8. Ahn KT, Song YB, Choe YH, et al. Impact of transmural necrosis on left ventricular remodeling and clinical outcomes in patients undergoing primary percutaneous coronary intervention for ST-segment elevation myocardial infarction. *The International Journal of Cardiovascular Imaging* 2013; **29(4)**: 835-842.
9. Berti V, Sciagrà R, Acampa W, et al. Relationship between infarct size and severity measured by gated SPECT and long-term left ventricular remodelling after acute myocardial infarction. *European Journal of Nuclear Medicine and Molecular Imaging* 2011; **38(6)**: 1124-1131.
10. Kaul S. There may be more to myocardial viability than meets the eye! *Circulation* 1995; **92(10)**: 2790-2793.
11. Ashikaga H, Mickelsen SR, Ennis DB, et al. Electromechanical analysis of infarct border zone in chronic myocardial infarction. *American Journal of Physiology-Heart and Circulatory Physiology* 2005; **289(3)**: H1099-H1105.
12. Notomi Y, Setser RM, Shiota T, et al. Assessment of left ventricular torsional deformation by Doppler tissue imaging validation study with tagged magnetic resonance imaging. *Circulation* 2005; **111(9)**: 1141-1147.
13. Helm P, Beg MF, Miller MI, Winslow RL. Measuring and mapping cardiac fiber and laminar architecture using diffusion tensor MR imaging. *Annals of the New York Academy of Sciences* 2005; **1047(1)**: 296-307.
14. Dall'Armellina E, Karia N, Lindsay AC, et al. Dynamic changes of edema and late gadolinium enhancement after acute myocardial infarction and their relationship to functional recovery and salvage index. *Circulation: Cardiovascular Imaging* 2011; **4(3)**: 228-236.
15. Zhang Z, Tendulkar A, Sun K, et al. Comparison of the Young-Laplace law and finite element based calculation of ventricular wall stress: implications for postinfarct and

surgical ventricular remodeling. *The Annals of Thoracic Surgery* 2011; **91(1)**: 150-156.
16. Kerckhoffs RC, McCulloch AD, Omens JH, Mulligan LJ. Effects of biventricular pacing and scar size in a computational model of the failing heart with left bundle branch block. *Medical Image Analysis* 2009; **13(2)**: 362-369.
17. Fomovsky GM, Macadangdang JR, Ailawadi G, Holmes JW. Model-based design of mechanical therapies for myocardial infarction. *Journal of Cardiovascular Translational Research* 2011; **4(1)**: 82-91.
18. Shimkunas R, Zhang Z, Wenk JF, et al. Left ventricular myocardial contractility is depressed in the borderzone after posterolateral myocardial infarction. *The Annals of Thoracic Surgery* 2013; **95(5)**: 1619-1625.
19. Lee PT, Dweck MR, Prasher S, et al. Left ventricular wall thickness and the presence of asymmetric hypertrophy in healthy young army recruits: data from the LARGE heart study. *Circulation: Cardiovascular Imaging* 2013; **6**: 262-267.
20. Nash MP, Panfilov AV. Electromechanical model of excitable tissue to study reentrant cardiac arrhythmias. *Progress in Biophysics and Molecular Biology* 2004; **85(2)**: 501-522.
21. Ashikaga H, Coppola BA, Hopenfeld B, Leifer ES, McVeigh ER, Omens JH. Transmural dispersion of myofiber mechanics: implications for electrical heterogeneity in vivo. *Journal of the American College of Cardiology* 2007; **49(8)**: 909-916.
22. Walker JC, Ratcliffe MB, Zhang P, et al. MRI-based finite-element analysis of left ventricular aneurysm. *American Journal of Physiology-Heart and Circulatory Physiology* 2005; **289(2)**: H692-H700.
23. Potse M, Dubé B, Richer J, Vinet A, Gulrajani RM. A comparison of monodomain and bidomain reaction-diffusion models for action potential propagation in the human heart. *Biomedical Engineering, IEEE Transactions on* 2006; **53(12)**: 2425-2435.
24. Ramanathan C, Jia P, Ghanem R, Ryu K, Rudy Y. Activation and repolarization of the normal human heart under complete physiological conditions. *Proceedings of the National Academy of Sciences* 2006; **103(16)**: 6309-6314.
25. Rice JJ, Wang F, Bers DM, De Tombe PP. Approximate model of cooperative activation and crossbridge cycling in cardiac muscle using ordinary differential equations. *Biophysical Journal* 2008; **95(5)**: 2368-2390.
26. Mitchell JR, Wang J-J. Expanding application of the Wiggers diagram to teach cardiovascular physiology. *Advances in Physiology Education* 2014; **38(2)**: 170-175.
27. Leong CN, Al Abed A, Lim E, et al. Electromechanics modeling of the effects of myocardial infarction on left ventricular function. Paper presented at: Engineering in Medicine and Biology Society (EMBC), 2015 37th Annual International Conference of the IEEE2015.
28. Becker M, Ocklenburg C, Altiok E, et al. Impact of infarct transmurality on layer-specific impairment of myocardial function: a myocardial deformation imaging study. *European Heart Journal* 2009; **30(12)**: 1467-1476.
29. Hiesinger W, Brukman MJ, McCormick RC, et al. Myocardial tissue elastic properties determined by atomic force microscopy after stromal cell–derived factor 1α angiogenic therapy for acute myocardial infarction in a murine model. *The Journal of Thoracic and Cardiovascular Surgery* 2012; **143(4)**: 962-966.
30. Gupta KB, Ratcliffe MB, Fallert MA, Edmunds L, Bogen DK. Changes in passive mechanical stiffness of myocardial tissue with aneurysm formation. *Circulation* 1994; **89(5)**: 2315-2326.

31. Abd-Elmoniem KZ, Tomas M, Sasano T, et al. Assessment of distribution and evolution of Mechanical dyssynchrony in a porcine model of myocardial infarction by cardiovascular magnetic resonance. *Journal of Cardiovascular Magnetic Resonance* 2012; **14(1)**: 1-10.
32. Watanabe H, Sugano T, Sugiura S, Hisada T. Finite element analysis of ventricular wall motion and intra-ventricular blood flow in heart with myocardial infarction. *JSME International Journal Series C Mechanical Systems, Machine Elements and Manufacturing* 2004; **47(4)**: 1019-1026.
33. Wang J, Khoury DS, Yue Y, Torre-Amione G, Nagueh SF. Preserved left ventricular twist and circumferential deformation, but depressed longitudinal and radial deformation in patients with diastolic heart failure. *European Heart Journal* 2008; **29(10)**: 1283-1289.
34. Lang RM, Bierig M, Devereux RB, et al. Recommendations for chamber quantification. *European Heart Journal-Cardiovascular Imaging* 2006; **7(2)**: 79-108.
35. Anversa P, Loud AV, Levicky V, Guideri G. Left ventricular failure induced by myocardial infarction. I. Myocyte hypertrophy. *American Journal of Physiology-Heart and Circulatory Physiology* 1985; **248(6)**: H876-H882.
36. Creemers EE, Pinto YM. Molecular mechanisms that control interstitial fibrosis in the pressure-overloaded heart. *Cardiovascular Research* 2011; **89(2)**: 265-272.
37. Blom AS, Mukherjee R, Pilla JJ, et al. Cardiac support device modifies left ventricular geometry and myocardial structure after myocardial infarction. *Circulation* 2005; **112(9)**: 1274-1283.
38. Nelson DM, Ma Z, Fujimoto KL, Hashizume R, Wagner WR. Intra-myocardial biomaterial injection therapy in the treatment of heart failure: Materials, outcomes and challenges. *Acta Biomaterialia* 2011; **7(1)**: 1-15.
39. Dor V. The endoventricular circular patch plasty ("Dor procedure") in ischemic akinetic dilated ventricles. *Heart Failure Reviews* 2001; **6(3)**: 187-193.
40. McDonald KS, Hanft LM, Domeier TL, Emter CA. Length and PKA dependence of force generation and loaded shortening in porcine cardiac myocytes. *Biochemistry Research International* 2012; 371415-371415.
41. Weiss DL, Ifland M, Sachse FB, Seemann G, Dössel O. Modeling of cardiac ischemia in human myocytes and tissue including spatiotemporal electrophysiological variations/Modellierung kardialer Ischämie in menschlichen Myozyten und Gewebe. *Biomedizinische Technik/Biomedical Engineering* 2009; **54(3)**: 107-125.
42. Wall ST, Guccione JM, Ratcliffe MB, Sundnes JS. Electromechanical feedback with reduced cellular connectivity alters electrical activity in an infarct injured left ventricle: a finite element model study. *American Journal of Physiology-Heart and Circulatory Physiology* 2012; **302(1)**: H206-H214.
43. Jie X, Gurev V, Trayanova N. Mechanisms of mechanically induced spontaneous arrhythmias in acute regional ischemia. *Circulation Research* 2010; **106(1)**: 185-192.

TABLES

Table 1. LV model parameter values

Parameter	Value
Reference (i.e. zero-strain) Geometry	
Inner ellipsoid minor semi-axis length	20.29 mm
Inner ellipsoid major semi-axis length	40.58 mm
Basal wall thickness	13.33 mm
Apex wall thickness	3.22 mm
Electrophysiology Formulations	
a	0.1
b	0.1
c	200 s^{-1}
k	1600 s^{-1}
ε	0.01
μ_1	0.12
μ_2	0.3
I_s	2
D_f	35e-3 m^2/s
D_t	4.7e-3 m^2/s
Passive Mechanical Properties	
C_0	0.090 kPa
b_f	24.63
b_t	9.63
b_{fa}	8.92
p	1 MPa
Active Contraction Formulations	
l_0	1.9 μm
T_0	0.2 kPa
A_3	309.5 μm^{-3}
A_2	-1497.3 μm^{-2}
A_1	2428.6 μm^{-1}
A_0	-1320.2
τ_0	0.01
m_τ	0.0604 μm^{-1}
c_τ	-0.0719
n_0	6.5
m_n	-0.5257 μm^{-1}
c_n	1.9744
Windkessel Properties	
R_c	0.04 mmHg*s/ml
R_p	1.18 mmHg*s/ml
C_p	0.39 ml/mmHg
Infarct Properties	
C_0	0.270 kPa
D_f	75e-5 m^2/s
D_t	3.5e-5 m^2/s
T_0	0 Pa

Table 2. Infarct properties of simulated models

Model	Infarct Volume (cm^3)	Endocardial Area Covered (cm^2)	TME (%)
TR10	1.46	11.17	10
TR24	3.58	11.10	24
TR51	7.52	11.10	51
TR75	11.22	11.15	75
TR100	14.92	11.15	100

Table 3. Simulated hemodynamic values. EDV: end-diastolic volume; ESV: end-systolic volume; SV: stroke volume; EF: ejection fraction; P_{sys}: peak systolic pressure; **NORMAL**: non-infarcted LV; **TR10**, **TR24**, **TR51**, **TR75** and **TR100**: Infarcted LV with varying transmural extent of the infarct

Model	EDV (ml)	ESV (ml)	SV (ml)	EF (%)	P_{sys} (mmHg)
NORMAL	118.7	49.9	68.8	58	120.5
TR10	115.6	51.0	64.6	56	117.0
TR24	115.6	52.0	63.6	55	115.2
TR51	115.2	54.6	60.6	53	110.6
TR75	114.9	57.2	57.7	50	107.0
TR100	114.8	59.0	55.8	49	106.1

FIGURES

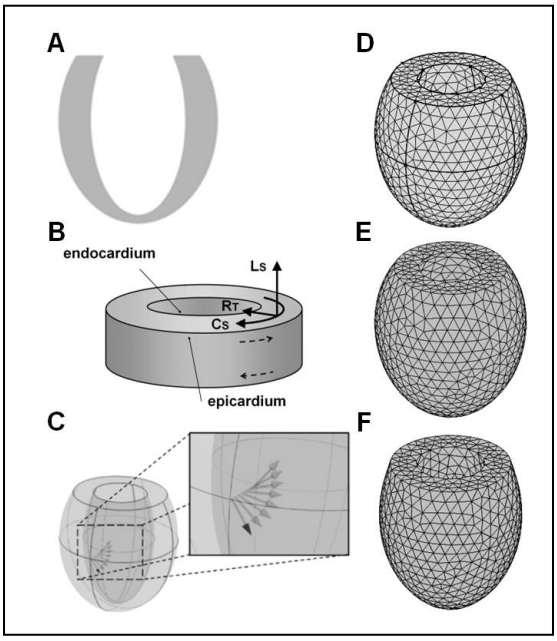

Fig. 1. A: Reference geometry of the LV model. B: Circumferential (C_S), longitudinal (L_S) and radial (R_T) directions defined on the myocardium. C: Transmural distribution of the fiber orientation. D: Undeformed mesh of the model. E: Deformed mesh at end-diastole. F: Deformed mesh at end-systole.

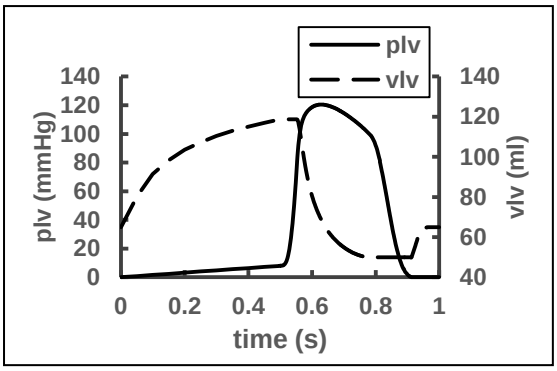

Fig. 2. Time course of *plv* and *vlv* obtained for the **NORMAL** model. *plv*: left ventricular pressure; *vlv*: left ventricular cavity volume.

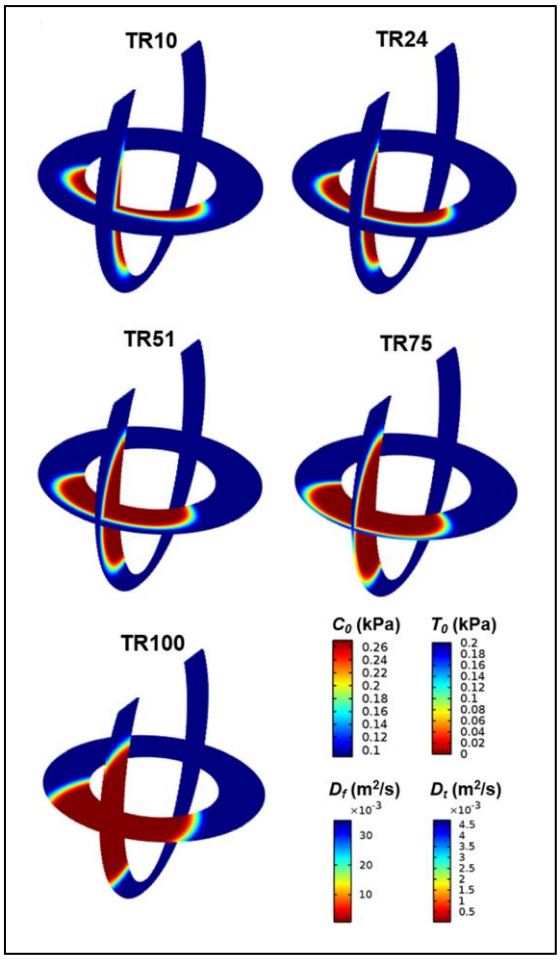

Fig. 3. Generated infarct models with varying TME of the infarct. The scales show the properties of the myocardium (C_0, T_0, D_f, and D_t), with blue and red colors represent RZ and IZ respectively, whilst color in between the two denotes the transition of BZ from RZ to IZ.

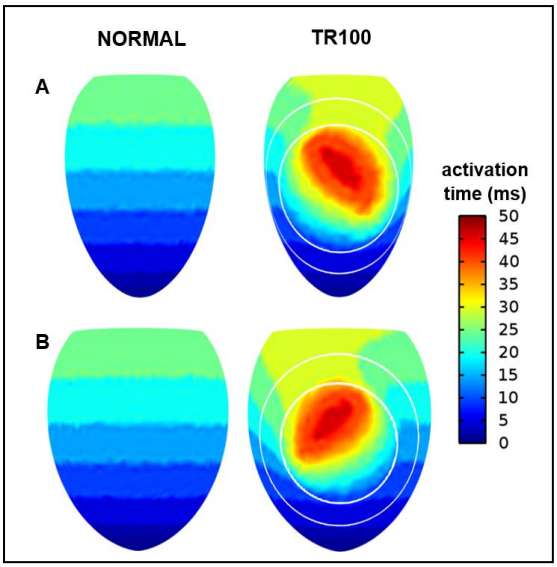

Fig. 4. Simulated activation times of subendocardium (A) and subepicardium (B) for the **NORMAL** and **TR100** models.

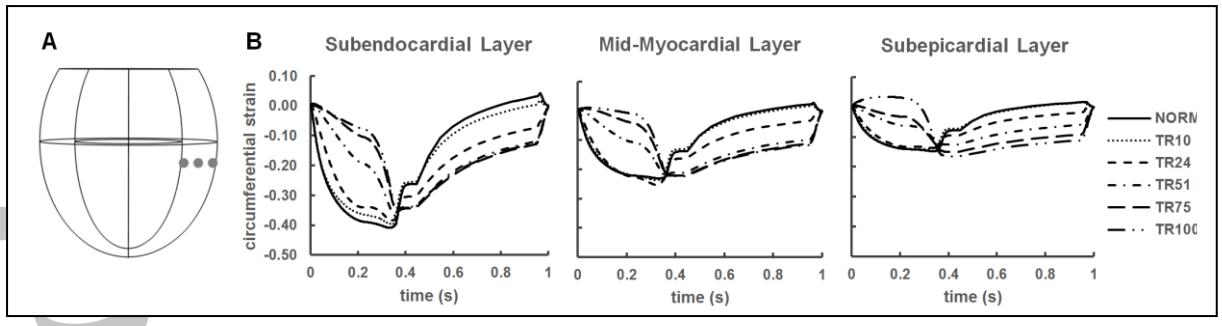

Fig. 5. A: Selected point in each layer of the myocardium for generating time course of circumferential strain. B: Simulated time course of circumferential strain in each myocardial layer.

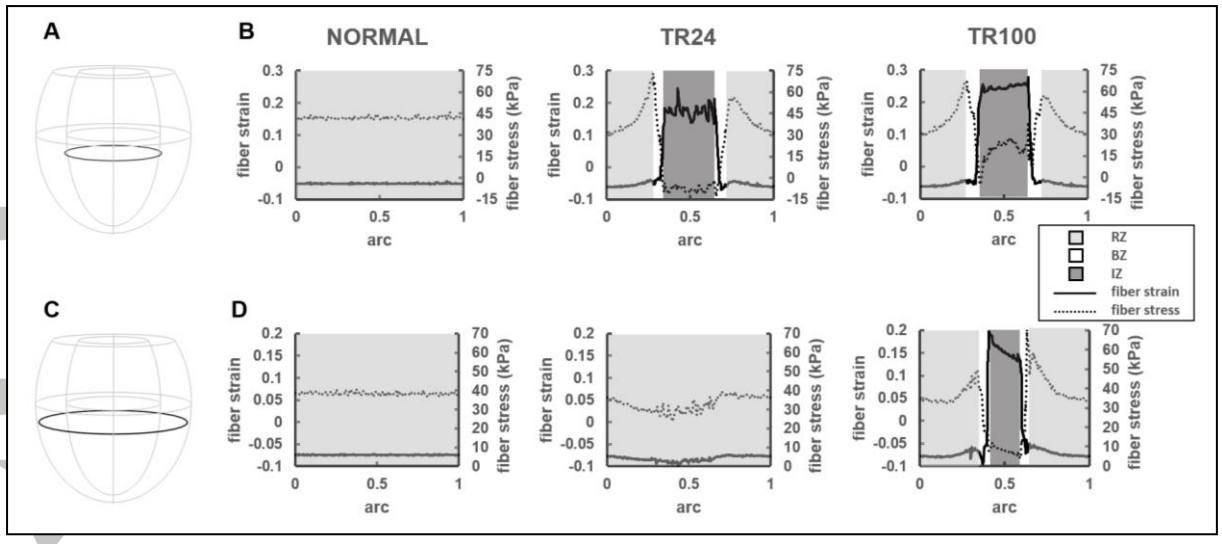

Fig. 6. Circumferential rings spanning around subendocardial (A) and subepicardial (C) layers used to generate Figs. 6B and 6D respectively. Fiber strain and stress distributions across the subendocardial (B) and subepicardial (D) layers of the **NORMAL**, **TR24** and **TR100** models.

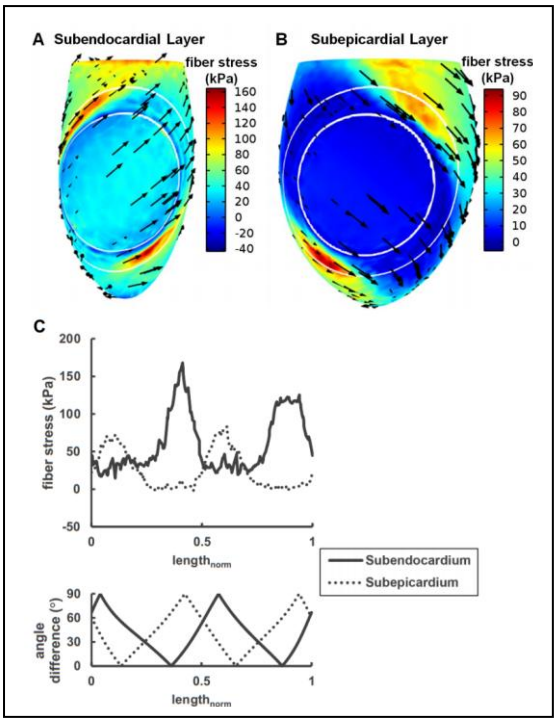

Fig. 7. Fiber stress distributions for the subendocardial (A) and subepicardial (B) layers of model **TR100** during ES, with the IZ, BZ and RZ separated by white circles, whilst the fiber orientations are indicated by the black arrows. Arrowheads for the fiber orientation are arbitrarily chosen to point in a counterclockwise direction when viewed from the base. C: Fiber stress (top panel) versus angle difference between myocardial fiber and BZ-RZ boundary (bottom panel) plotted along the BZ-RZ boundary of the subendocardial and the subepicardial layers. $length_{norm}$: normalized length along the BZ-RZ boundary

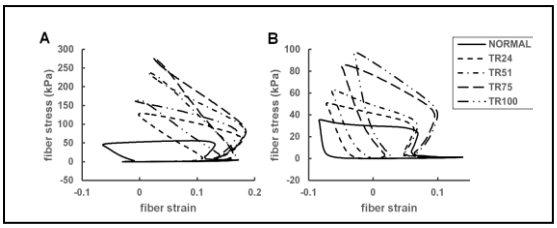

Fig. 8. Stress-strain loops of models with varying infarct TME, taken from the maximum stress points in the subendocardial (A) and subepicardial (B) layers.

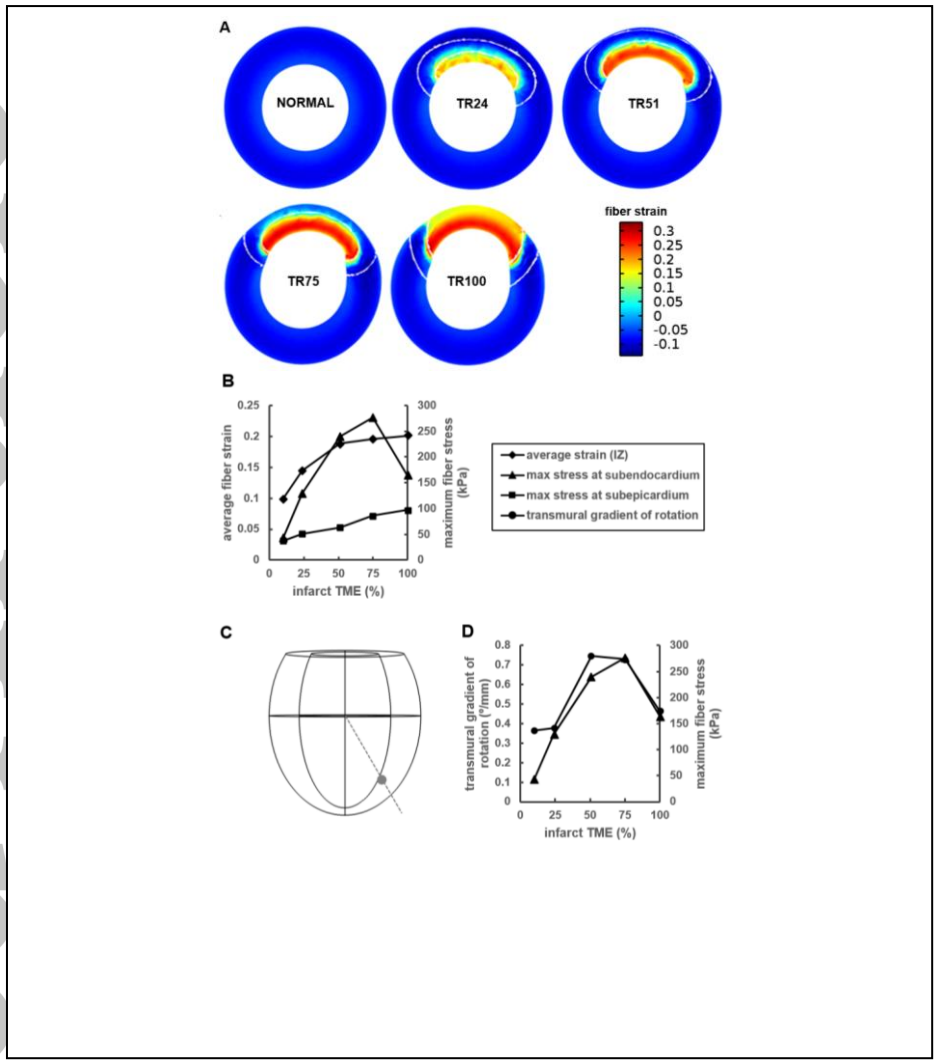

Fig. 9. ES fiber strain distribution of the simulated models in short axis view (A). Average ES fiber strain in the IZ, the maximum fiber stress in the subendocardial and subepicardial layers with increasing TME of the infarct (B), as well as the correlation between the maximum fiber stress in the subendocardial layer and its transmural gradient of rotation (D), derived along the dashed line shown in (C).

Mini Abstract

This work examines the mechanical interaction between the viable and ischemic myocardium in the presence of varying infarct transmural extent to better understand the mechanisms leading to infarct extension. Simulations using a 3D electromechanical model incorporating realistic fibre orientation demonstrated localized highly abnormal systolic fiber stress at the border zone, owing to the simultaneous presence of high strain and stiffness at this region. Apart from elevating fiber stress at the border zone through mechanical tethering imposed by the infarct zone, increasing infarct transmural extent also increases energy expenditure and reduces energy efficiency.

High fiber stress at BZ regions with fiber direction tangential to the IZ-BZ boundary.

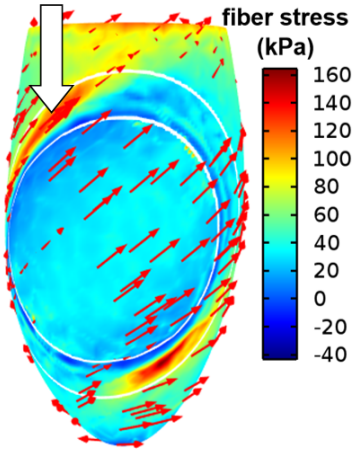

High fiber stress at BZ caused by mechanical interaction between ischemic and viable myocardium.